

All-Optical Signal Processing of Vortex Beams with Diffractive Deep Neural Networks

Zebin Huang,^{1,†} Peipei Wang,^{1,†} Junmin Liu,² Wenjie Xiong,¹ Yanliang He,¹ Jiangnan Xiao,³ Huapeng Ye,⁴ Ying Li,¹ Shuqing Chen^{1,*}, and Dianyuan Fan¹

¹*International Collaborative Laboratory of 2D Materials for Optoelectronics Science and Technology of Ministry of Education, Institute of Microscale Optoelectronics, Shenzhen University, Shenzhen 518060, China*

²*College of New Materials and New Energies, Shenzhen Technology University, Shenzhen 518118, China*

³*Terahertz Technology Innovation Research Institute, Shanghai Key Lab of Modern Optical System, Terahertz Science Cooperative Innovation Center, School of Optical-Electrical Computer Engineering, University of Shanghai for Science and Technology, Shanghai 200093, China*

⁴*Guangdong Provincial Key Laboratory of Optical Information Materials and Technology & Institute of Electronic Paper Displays, South China Academy of Advanced Optoelectronics, South China Normal University, Guangzhou 510006, China*

(Received 9 September 2020; revised 2 November 2020; accepted 8 December 2020; published 21 January 2021)

Vortex beams (VBs), possessing a helical phase front and carrying orbital angular momentum (OAM), have attracted considerable attention in optical communications for their mode orthogonality. A platform for achieving all-optical signal processing of VBs, however, remains elusive due to the limited light-field-manipulation capability. We introduce diffractive deep neural networks (D²NNs) and their applications to process VBs. Exploiting the multiple-light-field-modulation ability of multilayer diffraction structures and the strong data-processing capability of deep neural networks, we reveal that D²NNs can manipulate multiple VBs by configuring the phase and amplitude distribution of diffractive screens. The diffraction efficiency and converted-mode purity are greater than 96%. After being trained, D²NNs with functions of hybrid-OAM-mode generation, identification, and conversion are obtained, and three typical types of all-optical signal-processing communication, (OAM-shift keying (OAM-SK), OAM multiplexing and demultiplexing, and OAM-mode switching) are successfully achieved. Our simulation results provide an approach that breaks the limitations of poor functionality and complex design in processing VBs, introducing the D²NN as a universal light-field-modulation platform.

DOI: 10.1103/PhysRevApplied.15.014037

I. INTRODUCTION

Vortex beams (VBs), possessing a helical phase front described by the phase factor $\exp il\theta$, have been proved to carry an orbital angular momentum (OAM) of $l\hbar$ per photon, where l is the topological charge representing the OAM mode, θ is the azimuth angle, and \hbar is the Planck constant divided by 2π [1]. This nonuniform field distribution endows VBs with many unique optical characteristics, attracting broad interest in optical tweezers [2,3], quantum-information processing and quantum entanglement [4,5], optical trapping [6], optical communication [7–15], etc. VBs with different OAM modes are mutually orthogonal, which offers an additional physical dimension for optical communication in increasing transmission capacity. Mapping digital signals to OAM modes, researchers realized

OAM-shift-keying (OAM-SK) communication via rapidly switching OAM modes [15]. The multiplexing communication transmits multiple VBs in one physical channel, and the communication-capacity density will be significantly enhanced by increasing the number of multiplexed VBs [16–18]. Besides, the OAM mode of VBs can be exchanged by passive optical devices, which provides an efficient way for signal switching [19]. The modulation of VBs is ubiquitous in OAM-SK multiplexing, and optical switching, but conventional passive optical devices are available only for limited OAM modes, which restricts their application in optical communications and all-optical networks.

Various devices, including a spiral phase plate [20], a spatial light modulator [16,17,19], and a metasurface [21–31], have been widely investigated for manipulating VBs. The spiral phase plate with azimuthally rotated optical thickness modulates the spatial phase of light beams via introducing phase differences to the wave front and has been used to produce VBs due to its simple structure and

*shuqingchen@szu.edu.cn

†Zebin Huang and Peipei Wang contributed equally to this work.

easy fabrication. However, the fixed structure makes it possess limited modulation ability. Writing signals via electrical or optical addressing to change the optical characteristics, a spatial light modulator can flexibly adjust the phase and amplitude of VBs. But the prescient phase-modulation signals require electro-optical conversion, resulting in a low modulation rate and poor integration. A metasurface, a two-dimensional metamaterial with subwavelength structure, modulates the wave front of light beams by manipulating the arrangement of materials and microstructures [32–40]. Although a metasurface can accurately manipulate light fields, it is difficult to simultaneously modulate multiple VBs, resulting in reduced functionality. Besides, these methods are usually single-layer phase-modulation methods, which have limited modulation capability to perform complex wave-front processing in multiple light fields.

Multilayer diffraction methods cascading multiple diffractive screens empower complex phase-modulation functions. However, inverse designs or algorithms are required to determine the profile of each diffraction screen in advance. Wave-front-matching algorithms are used to calculate the phase distributions of multiple diffractive screens [41–44]. The forward and backward propagation of the input basis and desired output basis determine each phase mask, and the matching masks are obtained by setting phase iteration update rules. However, different matching principles must be designed for modulation tasks. Even worse, with the number of modes exceeding number of the phase screens, the light-processing capability will significantly decrease because of the excessive information required to be matched and the lack of efficient optimization-function assistance [41]. Recently, an all-optical diffractive deep neural network (D^2NN) combining the rich light-processing functions of multilayer diffraction and the learning, memory, and excellent information-processing ability of deep learning was proposed and applied in classification of Modified National Institute of Standards and Technology (MNIST), an open resource handwritten digit database, holographic imaging, and all-optical saliency detection [45–52]. With the powerful optimization functions and strong mapping capabilities, these D^2NN methods can precisely optimize the modulation parameters of each grid in diffractive screens and affect the wave front of secondary wave sources to output light fields via coherent superimposition. Unfortunately, they are applicable for target-classification tasks and consider only intensity distributions.

In this work, we introduce D^2NNs to manipulate VBs, aiming to provide a comprehensive platform for light-field processing. Composed of multiple diffractive layers with learnable grid phase and amplitude parameters, the abundant neurons enable D^2NNs to manipulate the light field with multiple OAM modes. By minimizing the loss between the predicted output field and the ideal

output field and inversely optimizing the structural parameters of diffraction layers, D^2NNs with optimal phase and amplitude distributions are trained for processing complex light fields. Focusing on effective features, D^2NNs can realize the mode conversion between different light fields and achieve multiple modulation functions via changing the input and desired output bases. Through the training of a five-layer D^2NN with mode- and spatial-location-conversion capabilities, single or hybrid OAM modes with $l \in [-4, +4]$ and Gaussian modes at different positions are mutually converted, and different OAM modes can be exchanged, which results in D^2NN functions for generating, detecting, and switching multiple OAM modes. Even if the mode range extends to $[-8, +8]$, the diffraction efficiency and mode conversion purity are greater than 96%. Constructing and simulating three typical types of all-optical signal-processing communication, OAM-shift keying, OAM multiplexing, and OAM-mode switching, we demonstrate that the bit error rates (BERs) are all below 10^{-4} . The D^2NN method offers an alternative solution for light-field manipulation, which may have potential for all-optical signal processing, optical communication, interconnection, etc.

II. LIGHT-FIELD PROCESSING WITH D^2NNs

The D^2NN possessing learning, memory, and light-field-processing abilities can be trained as a comprehensive platform for simultaneously manipulation of the mode and spatial location of light beams. Here we construct D^2NNs with updatable phase and amplitude parameters to modulate complex light fields (see Appendix A). Figure 1 shows a five-layer D^2NN , which is trained for processing VBs, including spatial-location conversion and mode exchange. A Laguerre-Gaussian beam with phase factor $\exp i\theta$ is used for simulating VBs with a working wavelength of 1550 nm and a radial index of zero [53]. The training period and learning rate are set as 2000 and 0.01, respectively. We first convert VBs to spatially separated Gaussian beams. As shown in Fig. 2, VBs with $l \in [-4, +4]$ and Gaussian beams with different spatial locations are set as the training input dataset and ideal output dataset,

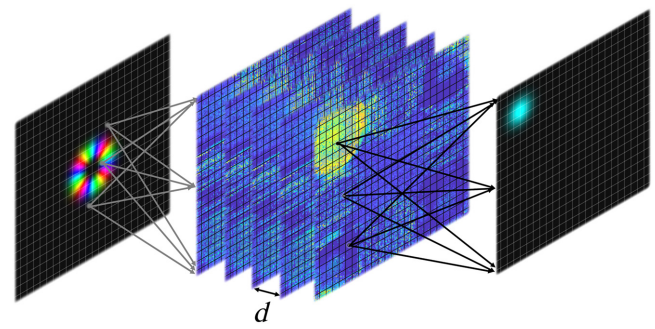


FIG. 1. The five-layer D^2NN .

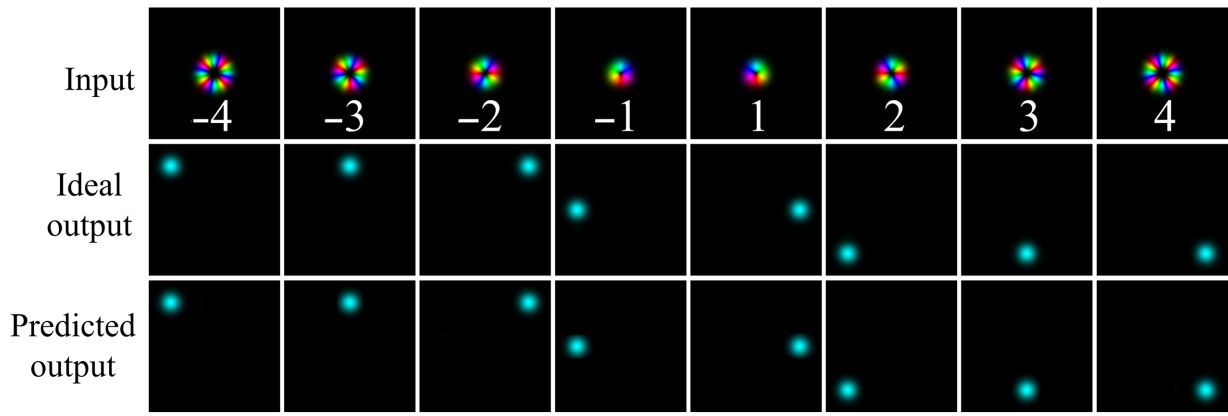


FIG. 2. Results for converting VBs to spatially separated Gaussian beams.

respectively. The constructed five-layer D²NN will automatically establish a conversion relationship and update the phase and amplitude distributions of diffractive layers. With training, the predicted output light fields are highly consistent with the ideal output (see Fig. 2), and the training process takes about 10 min with the graphics-processing unit of a NVIDIA GeForce GTX 1080 Ti. The predicted phase and amplitude distributions are shown in Fig. 3(a). The conversion of the D²NN can be expressed by

$$f_{\text{out}}(x, y) = D(f_{\text{in}}(x, y)), \quad (1)$$

where $f_{\text{in}}(x, y)$ and $f_{\text{out}}(x, y)$ are the input and output light fields, D represents the transform function of D²NN.

To evaluate the conversion performance, the energy utilization of each OAM mode is monitored. The results demonstrate that all the diffraction efficiencies exceed 99% without our considering fabrication error and reflection

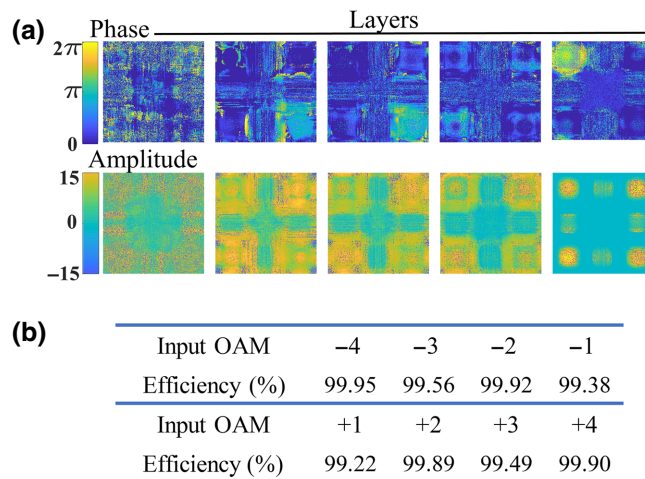


FIG. 3. Results for converting VBs to spatially separated Gaussian beams. (a) Phase and amplitude distributions of diffractive layers. (b) Efficiencies of output Gaussian beams. Here the unit of amplitude is mm.

[see Fig. 3(b)]. We use hybrid OAM modes as testing data to analyze the light-field-processing capability. The field distribution of input hybrid VBs can be expressed by

$$\begin{aligned} f_{\text{multiple}}(x, y) = & f_{\text{OAM1}}(x, y) + f_{\text{OAM2}}(x, y) + \dots \\ & + f_{\text{OAM}_n}(x, y), \end{aligned} \quad (2)$$

where $f_{\text{OAM}_n}(x, y)$ represents the input OAM mode included in the training set, where n is the number of modes, which is not larger than the size of the training set. The test results in Fig. 4 show that the D²NN can recognize the OAM modes of input hybrid VBs, which can also be converted to spatially separated Gaussian beams. Notably, the D²NN can process hybrid VBs with hybrid OAM modes except for single OAM modes in the training process. The modulation is expressed by

$$\begin{aligned} f_{\text{multiple_out}}(x, y) = & D_1(f_{\text{multiple_in}}(x, y)) \\ = & D_1(f_{\text{OAM1}}(x, y) + f_{\text{OAM2}}(x, y) \\ & + f_{\text{OAM3}}(x, y) + f_{\text{OAM4}}(x, y)) \\ = & f_{\text{Gaus1}}(x, y) + f_{\text{Gaus2}}(x, y) \\ & + f_{\text{Gaus3}}(x, y) + f_{\text{Gaus4}}(x, y), \end{aligned} \quad (3)$$

where $f_{\text{Gaus}}(x, y)$ represents the field distribution of the spatially separated Gaussian beam.

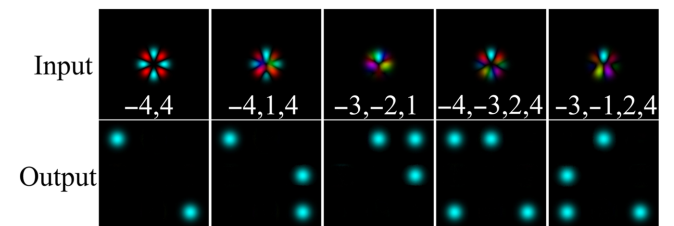


FIG. 4. Test results for converting the hybrid VB to spatially separated Gaussian beams.

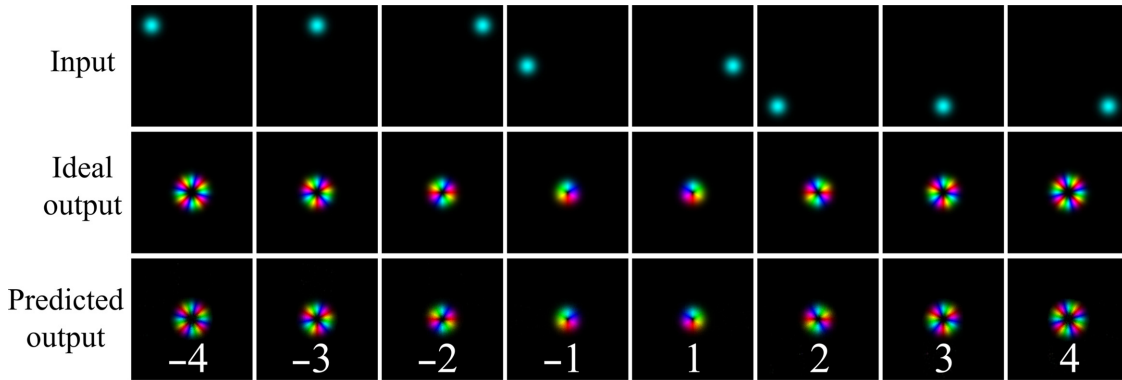


FIG. 5. Results for converting spatially separated Gaussian beams to VBSs.

Besides, we investigate the inverse conversion from Gaussian beams to VBSs. As shown in Fig. 5, the input training beams are eight Gaussian beams with different spatial locations, and VBSs with $l \in [-4, +4]$ are set as the ideal output data. After being trained, the D²NN can accurately modulate the input spatially separated Gaussian beams to target fields. The final phase and amplitude distributions of the five-layer diffractive screens are displayed in Fig. 6(a). The test results show that both the diffraction efficiency of the D²NN and the mode purity of VBSs are more than 99% [see Fig. 6(b)].

Similarly, the superimposed Gaussian beams are randomly combined as the testing data and propagate through the diffractive layers. As shown in Fig. 7, the D²NN can convert Gaussian beams to VBSs, even through the testing data are not considered in the training process, which

gives it the ability to produce hybrid VBSs and reduce the complexity of OAM-mode multiplexing.

Furthermore, we demonstrate the mode exchange of VBSs. Six sets of VBSs (shown in Fig. 8) with mode interval Δl from 1 to 3 are used as training data. After training, the mode exchange is realized, which can process light fields according to input OAM modes. The phase and amplitude distributions of the five-layer D²NN are shown in Fig. 9(a). The diffraction efficiency and converted-mode purity reach approximately 97% and 99%, respectively [see Fig. 9(b)]. Compared with conventional optical elements such as metasurfaces, the D²NN can process more OAM modes, which significantly increases the light-field-manipulation capability and decreases the system complexity.

III. ALL-OPTICAL SIGNAL PROCESSING OF VBSs WITH A D²NNs

To verify its light-field-manipulation capabilities, we use the previously trained D²NNs for optical communication, including OAM-SK, OAM multiplexing and demultiplexing, and OAM-mode switching.

A. OAM-SK

In OAM-SK communication, the digital signals are encoded into different OAM modes and decoded in the receiver for information recovery. The modulation capability depends on the accuracy of identifying OAM modes.

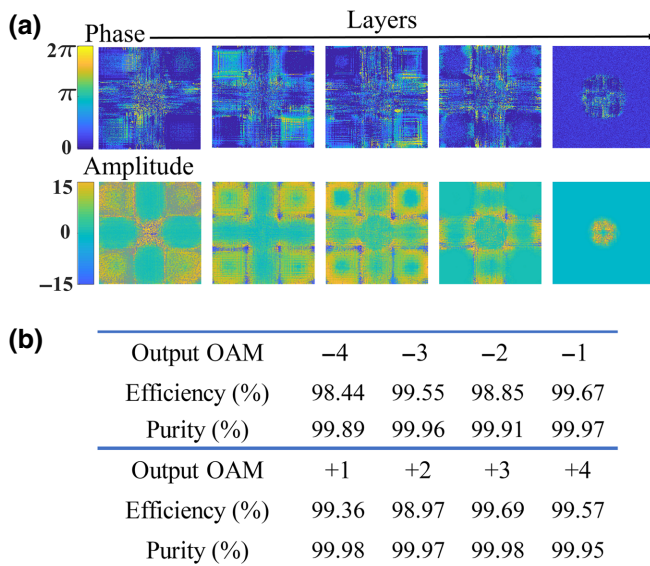


FIG. 6. Results for converting spatially separated Gaussian beams to VBSs. (a) Phase and amplitude distributions of diffractive layers. (b) Efficiencies and purities of output VBSs. Here the unit of amplitude is mm.

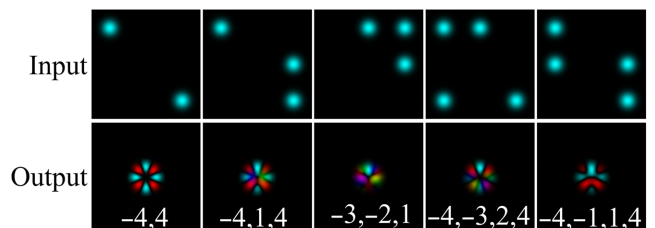
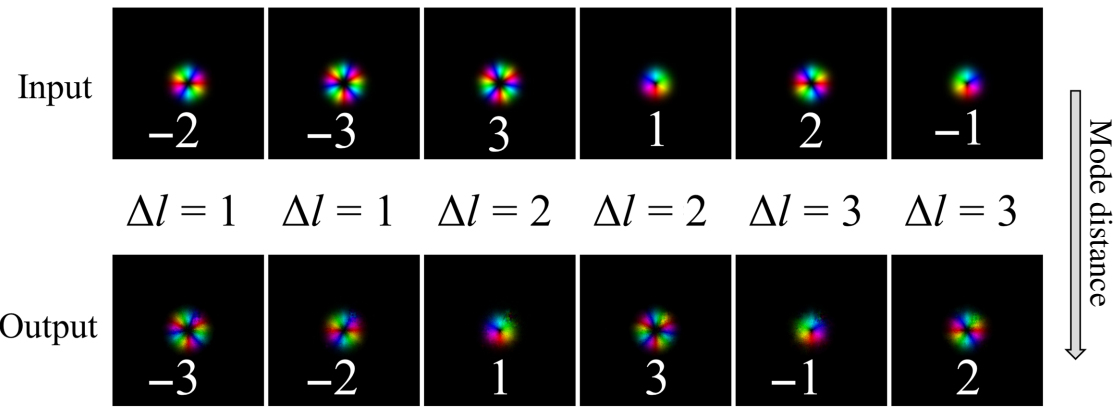


FIG. 7. Test results for converting superimposed Gaussian beams to multiple VBSs.

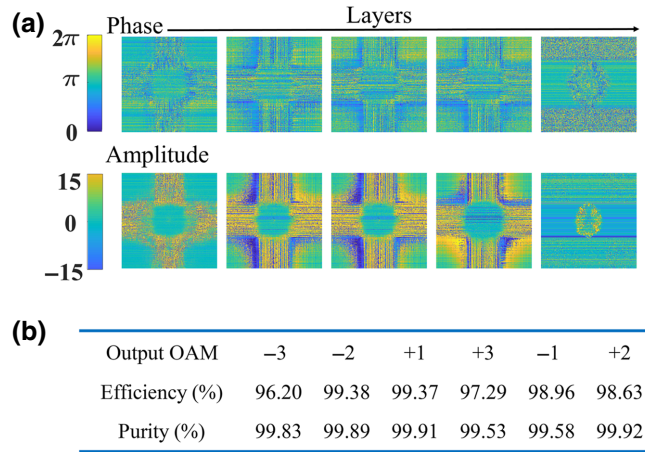
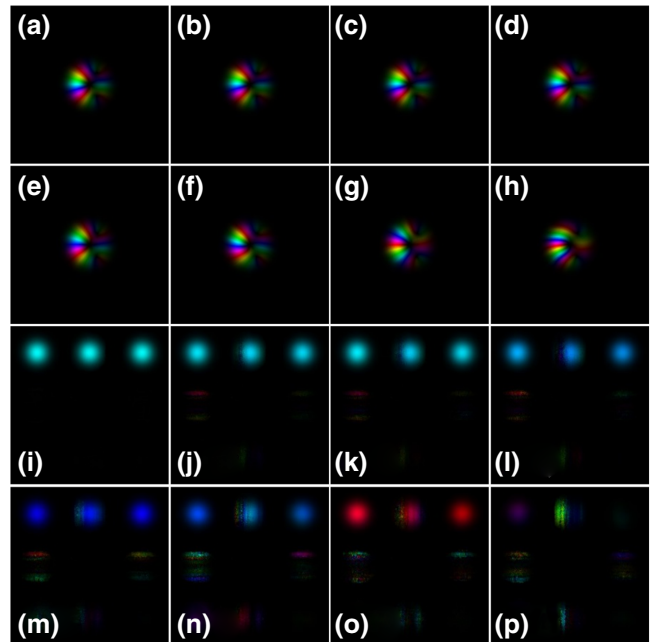
FIG. 8. Results for OAM-mode exchange with different mode distances (Δl).

However, conventional identifications are realized by classifying the intensity distributions of VBs, which makes it difficult to identify conjugate modes that have the same intensity distributions, and offline demodulation is required. The D²NN-based demodulator can demodulate shift-keying signals in real time.

To test the anti-interference ability, we introduce atmospheric turbulence to disturb VBs, and the Hill-Andrew turbulence model is used to simulate atmospheric turbulence [54]. The inner and outer scale of atmospheric turbulence are set as 0.2 mm and 50 m, respectively. Multiple VBs with $l = -4, -3, -2$ and different turbulence intensities ($C_n^2 \in [1 \times 10^{-16} \text{ m}^{-2/3}, 1 \times 10^{-13} \text{ m}^{-2/3}]$, $z=10 \text{ m}$) are inputted into the D²NN for mode processing, as shown in Figs. 10(b)–10(h). After demodulation, the hybrid VBs are converted to Gaussian beams [see Figs. 10(j)–10(p)]. These results indicate that the D²NN can resist weak turbulence [Figs. 10(j)–10(l)]. While under strong turbulence [Figs. 10(m)–10(p)] some energy is dispersed because the

D²NN is sensitive to both the phase and the amplitude distortions, it is still robust with regard to the distortions under moderate turbulence even though the phase distortions are not shown in the training.

We construct a 70-ary OAM-SK communication link, as shown in Fig. 11(a). A 100×100 grayscale image of the Shenzhen University emblem is encoded into 20 000 hybrid VBs (see Appendix B), and these then propagate 10 m under atmospheric turbulence. The D²NN

FIG. 9. Results for the mode exchange of VBs. (a) Phase and amplitude distribution of the D²NN. (b) Efficiencies and purities of the converted VBs. Here the unit of amplitude is mm.FIG. 10. Conversion results for hybrid OAM modes ($l = -4, -3, -2$) with atmospheric turbulence ($z=10 \text{ m}$). (a) VBs without atmospheric turbulence. (b) $C_n^2 = 1 \times 10^{-16} \text{ m}^{-2/3}$. (c) $C_n^2 = 5 \times 10^{-16} \text{ m}^{-2/3}$. (d) $C_n^2 = 1 \times 10^{-15} \text{ m}^{-2/3}$. (e) $C_n^2 = 5 \times 10^{-15} \text{ m}^{-2/3}$. (f) $C_n^2 = 1 \times 10^{-14} \text{ m}^{-2/3}$. (g) $C_n^2 = 5 \times 10^{-14} \text{ m}^{-2/3}$. (h) $C_n^2 = 1 \times 10^{-13} \text{ m}^{-2/3}$ (i)–(p) Output multiple Gaussian beams corresponding to different turbulence intensities.

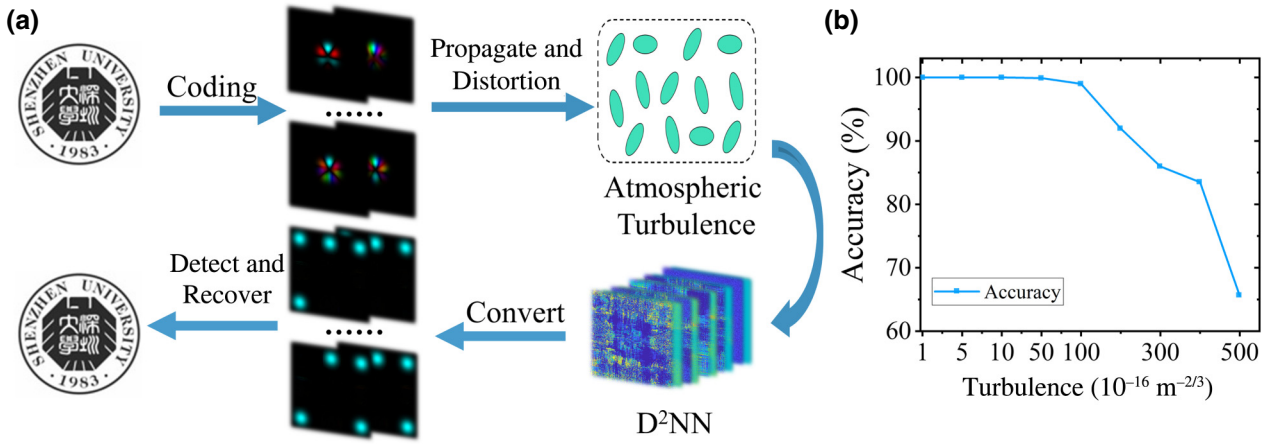


FIG. 11. (a) D²NN-based OAM-SK communication. (b) Demodulation accuracy for different atmospheric turbulences.

constructed as reported in the previous section is used to convert VBs to spatially separated Gaussian beams, and the intensity distributions are received for signal demodulation.

To explore the impact of transmission environments on the performance of OAM-SK communication, we introduce and simulate atmospheric turbulence with $C_n^2 \in [1 \times 10^{-16} \text{ m}^{-2/3}, 5 \times 10^{-14} \text{ m}^{-2/3}]$, and the propagation distance is 10 m. The demodulation-accuracy curve under different turbulence strengths is shown in Fig. 11(b); the errors of the calculations come mainly from turbulence distortion and the coding principle of OAM-shift-keying signals. Turbulence will cause errors in modulation and result in the dispersion of energy. For weak and moderate turbulences ($C_n^2 \in [1 \times 10^{-16} \text{ m}^{-2/3}, 1 \times 10^{-14} \text{ m}^{-2/3}]$), the D²NN can modulate the input light fields to output light fields with high conversion efficiency and low dispersion. Since the three regions of maximum light energy determine the OAM modes, if the light energy output at the right regions is dominant, the OAM modes can be accurately demodulated, which endows the D²NN-based modulator with a certain error tolerance, and the accuracy can be increased up to 100%. However, as the turbulence

strength increases, modulation becomes more difficult for severe phase distortion, which scatters most of the energy to wrong regions and results in non-negligible calculation errors in signal demodulation. What is worse, if any set of hybrid VBs is wrongly predicted, the D²NN cannot correctly decode the grayscale value in this pixel. Therefore, the accuracy decreases to 65.50% as the intensity increases to $5 \times 10^{-14} \text{ m}^{-2/3}$.

B. OAM multiplexing

Generally, the complexity of multiplexing systems is proportional to the number of multiplexing channels. Trained D²NNs possess the functions of converting VBs and spatially separating Gaussian beams, providing an efficient way for multichannel OAM multiplexing and demultiplexing and greatly simplifying the system. Figure 12 shows a diagram of OAM-multiplexing-demultiplexing communication with D²NNs, which is composed of the signal generation and multiplexing-demultiplexing modules. In the transmitter, a laser beam loaded with 16-quadrature-amplitude (16-QAM) signals produced by the signal generator is split into multiple sub-beams, which

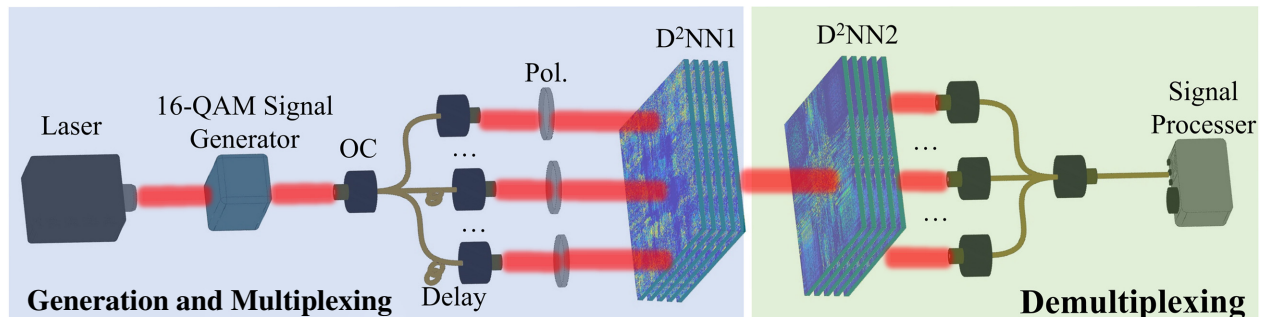


FIG. 12. D²NN-based OAM-multiplexing-demultiplexing communication. OC, optical coupler; Pol., polarizer.

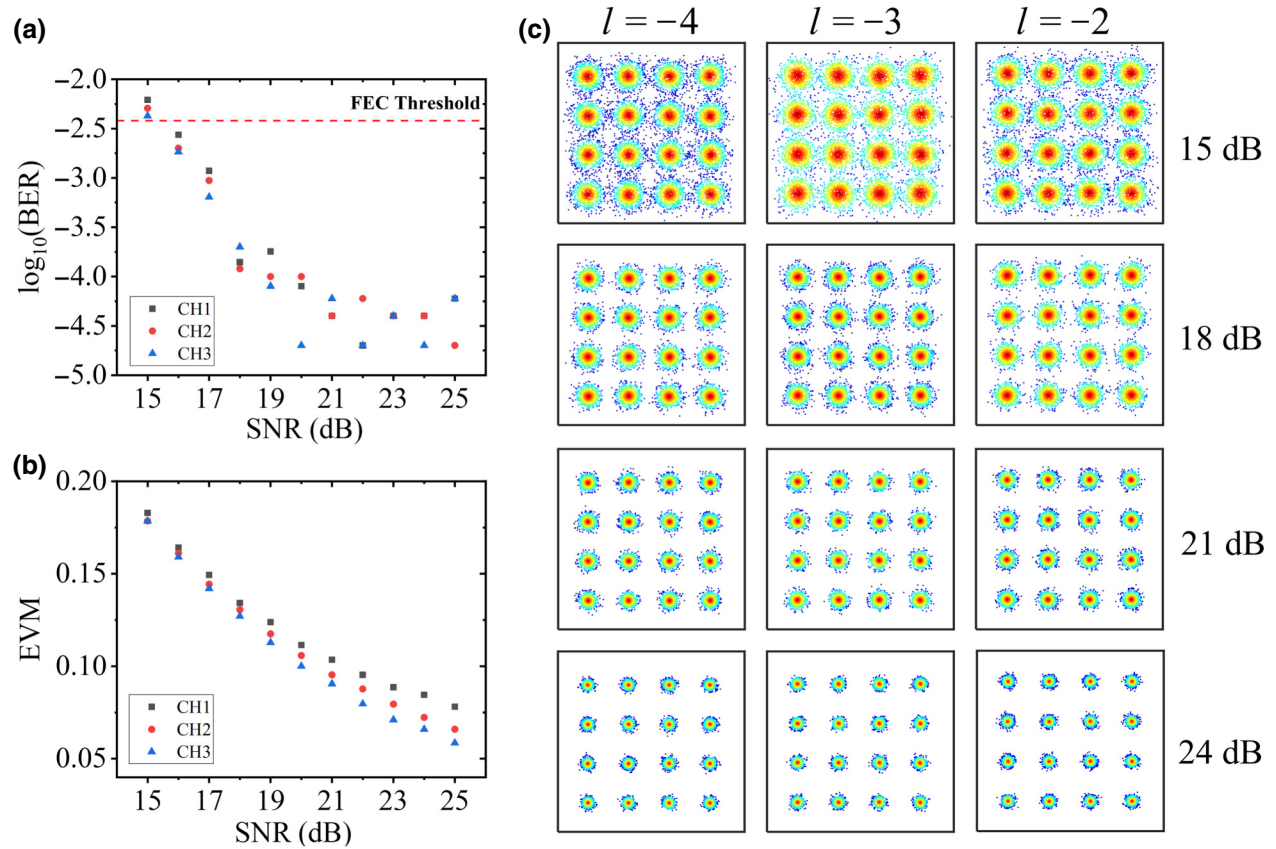


FIG. 13. Results for D^2NN -based three-channel OAM-multiplexing communication. (a) BER curves as a function of SNR for different channels. (b) EVM curves as a function of the SNR for different channels. (c) Constellations of different channels for different SNRs. FEC, forward error correction.

are delayed for decorrelation. All Gaussian sub-beams are inputted to D^2NN1 for OAM mode generation and channel multiplexing. After free-space transmission for 30 cm, the coaxial OAM channels are incident to D^2NN2 for synchronously demultiplexing multiple signals. The D^2NNs can accomplish the functions of generating, multiplexing, and demultiplexing OAM modes simultaneously, abolishing the need for additional devices and significantly decreasing the system complexity. We select three OAM modes with $l = -4, -3, -2$ to carry 16-QAM

signals, and multiplexing and demultiplexing are realized by D^2NNs . Here the waist radius of Gaussian sub-beams is 3 mm, the size and resolution of the plane are set as 30 mm and 256×256 , and the distance between Gaussian sub-beams on the horizontal axis is 10 mm.

Since channel noise will interfere with signals and increase the BER in communications, we use Gaussian white noise to disturb signals and use the signal-to-noise ratio (SNR) to represent the level of noise. Figure 13 shows the BER and error-vector magnitudes (EVMs) of the

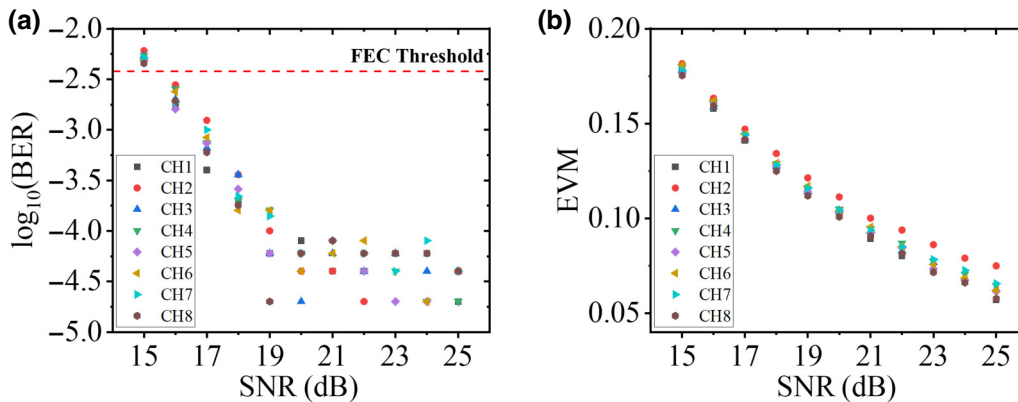


FIG. 14. Results for D^2NN -based eight-channel OAM-multiplexing-demultiplexing communication. (a) BER curve and (b) EVM curve. FEC, forward error correction.

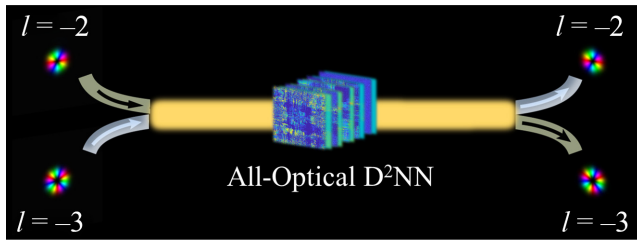


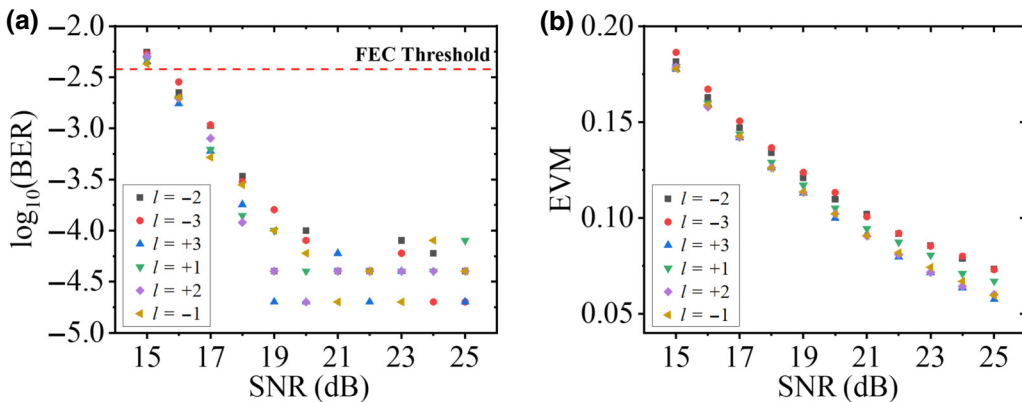
FIG. 15. OAM-mode-switching communication.

transmitted signals, which reflect the error of the demodulated signals in scalar and vector dimensions. CH1, CH2, and CH3 represent the OAM channels with $l = -4, -3, -2$, respectively. From Fig. 13, the BERs in all channels are below the forward-error-correction threshold (3.8×10^{-3}) except in the cases of SNR of 15 dB. When the SNR reaches 21 dB, the BERs decrease to 10^{-4} , and the EVMs of constellations decrease to 0.07.

The communication capacity of a multiplexing system depends on the number of multiplexed channels. To make full use of the information-processing capability of D²NNs, we increase the number of multiplexing channels from three to eight. These Gaussian beams are converted to VBS and superimposed for coaxial transmission, and are then decomposed and converted to Gaussian beams for signal demultiplexing. The curves of EVM and BER with different SNRs are shown in Fig. 14. When the SNR reaches 20 dB, the BERs of all channels are less than 10^{-4} , which indicates that the D²NN-based all-optical processing method can significantly reduce the system complexity and improve the communication performance of OAM multiplexing.

C. OAM-mode switching

OAM-mode switching, transferring signals from one OAM channel to another, is usually performed by a single optical element or multiple optical elements. For example, VBS with OAM modes of $l = a$ and $l = b$ can be exchanged by one reflective-type spatial light modulator loaded with



the same helical phases, which can be expressed by

$$E_{la} = E_{lb} \exp\{i[-(l_a + l_b)]\theta\}, \quad (4)$$

$$E_{lb} = E_{la} \exp\{i[-(l_a + l_b)]\theta\}, \quad (5)$$

where E_{la} and E_{lb} are the field distributions of the VBS with different OAM modes, and $-(l_a + l_b)$ represents the helical phase information loaded on the spatial light modulator. However, this method can exchange only two OAM modes and has limited processing ability. Besides, multiple spatial light modulators are required to increase the number of switching OAM modes, and it is difficult to find accurate phase-conversion-map relationships for arbitrary OAM modes.

The constructed D²NN can exchange multiple OAM modes with a nonuniform mode interval. For VBS with different OAM modes inputted coaxially, the D²NN can exchange the OAM modes (see Fig. 15). The results of three sets of mutual data exchange of VBS [$l = -2, -3$ ($|\Delta l| = 1$), $l = +3, +1$ ($|\Delta l| = 2$), and $l = +2, -1$ ($|\Delta l| = 3$)] with one D²NN are shown in Fig. 16. The BERs of all channels are below 10^{-4} with SNR of 20 dB, indicating that the D²NN has strong plasticity in mode exchange.

IV. DISCUSSION

The collimation of light beams is critical for the performance of optical systems, and most of optical-information processing devices are position sensitive, which require high alignment accuracy. For the D²NN, we divide the input plane into eight regions corresponding to eight spatially separated Gaussian beams. The incident shift of Gaussian beams may cause inaccurate light modulation, decreasing the diffraction efficiency and mode purity. The tolerance of position deviation is necessary for actual applications. To improve the fault tolerance for misalignment, we consider the deviation of the incident position in the training data set in advance. As shown in Fig. 17(a), eight sets of Gaussian beams are inputted into the D²NN

FIG. 16. Results for OAM-mode-switching communication. (a) BER curve and (b) EVM curve. FEC, forward error correction.

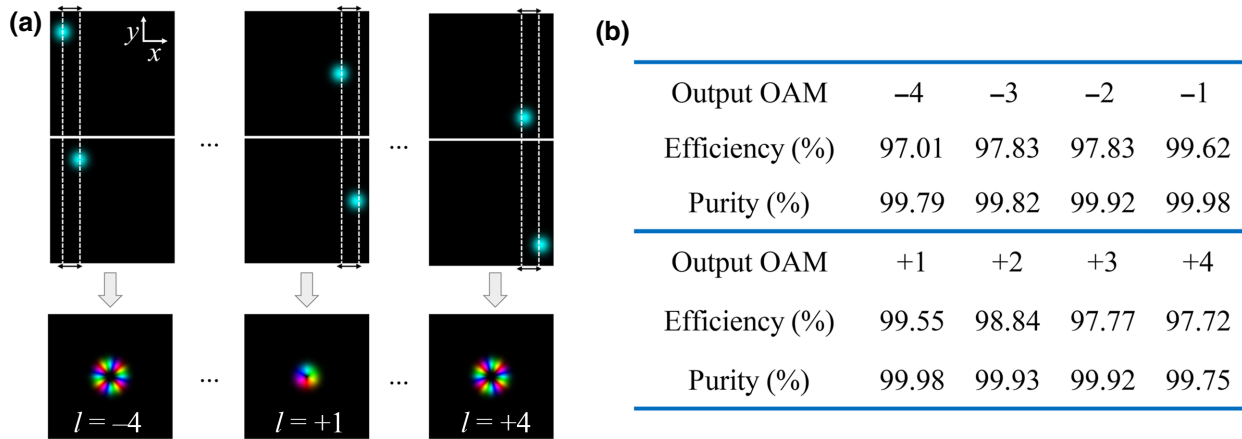


FIG. 17. Results for conversion from spatially shifted Gaussian beams to VBs. (a) Training data of Gaussian beams with the spatial shift on the x axis and VBs. (b) Efficiency and purity of different OAM modes.

to generate VBs, where each set of input data is composed of two Gaussian beams with and without a 4-mm spatial shift on the x axis. The structure, learning rate, and iteration period of the D²NN are set as the same as in the previous sections. After supervised training, the D²NN can convert all Gaussian beams to VBs in the eight regions, even if the incident position is changed. The D²NN can accurately complete all mode-interval modulation with $\Delta l \in (0, 4]$ by constructing a “two-to-one” mapping relationship between the input separated Gaussian beams and VBs, and the efficiency and mode purity of all OAM modes exceed 97% [see Fig. 17(b)]. Besides, we use a Gaussian beam (mapping the OAM of $l= -4$) with different shift distances as test data; the test results in Fig. 18 show that the purity of the converted VBs is inversely proportional to the minimum distance $\Delta d = \min(d_1, d_2)$, where d_1 represents the

distance between the input beam and the standard Gaussian beam, and d_2 represents the distance between the input beam and the Gaussian beam with a spatial shift of 4 mm. For a spatial shift of 2 mm, the mode purity is 95.37%, which is about 4% lower than for the standard Gaussian beam. This is because it is far from the incident position of the two Gaussian beams in the training set, making it difficult for the D²NN to accurately capture feature information. In addition, the transverse displacement should not be too large to avoid it being too close to the incident position of the Gaussian beam in adjacent regions, which causes mode crosstalk and reduces the modulation accuracy.

D²NNs can simultaneously modulate multiple VBs and realize OAM-mode multiplexing and demultiplexing in OAM communications. To further explore the all-optical processing ability, we increase the training data size to 16, including Gaussian beams with different input locations and VBs with $l \in [-8, +8]$. The structures are the same as in the previous section, both of which have five-layer diffractive screens with adjusted phase and amplitude distributions. After training, the D²NN can convert arbitrary hybrid VBs with multiple OAM modes with $l \in [-8, +8]$ superimposed, and the diffraction efficiency and converted-mode purity are greater than 96%. Constructing a 16-channel OAM multiplexing communication link, we use the trained D²NNs to multiplex and demultiplex 16 OAM channels carrying 16-QAM signals. The results in Fig. 19 show that the BERs of most channels are lower than the forward-error-correction threshold with SNR of 17 dB, and the EVMs of all channels decrease with the SNR as expected. These findings indicate that the D²NN has strong signal-processing capability in simultaneously converting modes and spatial locations.

With the development of near-field optics and the use of small-scale and large-angle light sources such as nanolasers, when the transmission distance comes close to the magnitude of the wavelength or is less than the

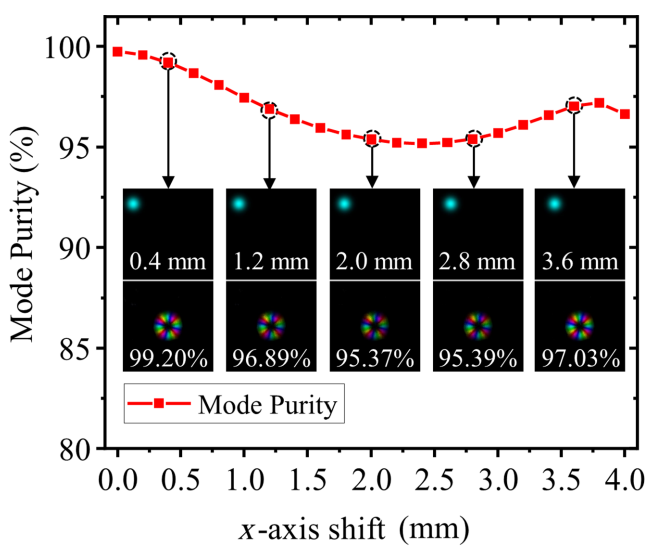


FIG. 18. Mode-purity curve as a function of spatial shift.

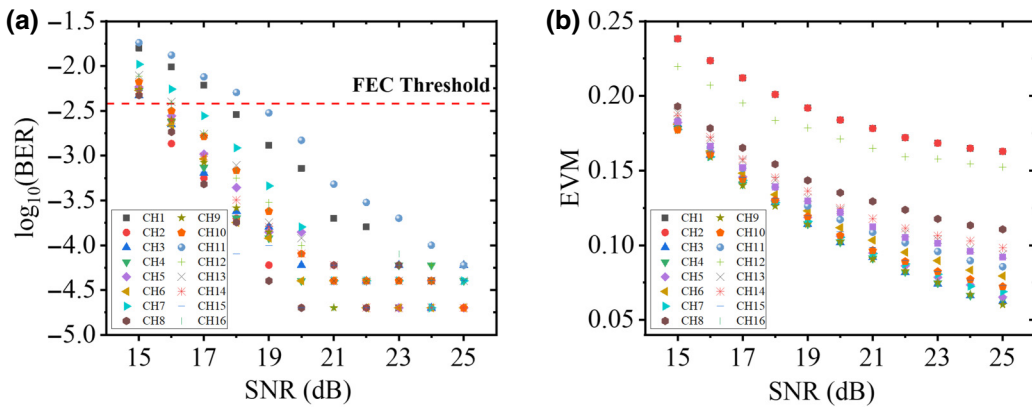


FIG. 19. Results for D²NN-based 16-channel-OAM-multiplexing-demultiplexing communication. (a) BER curve and (b) EVM curve. FEC, forward error correction.

wavelength, scalar diffraction theory will be no longer suitable for simulating light-field transmission, and vector diffraction theory should be used instead. In this work, scalar Fresnel diffraction theory is used to simulate the transmission of light beams (ignoring the polarization freedom) between the layers of the D²NN. However, it is necessary to replace it with vector angular spectrum theory or vector Rayleigh-Sommerfeld diffraction theory and consider multiple light-field-transmission components for the light-field modulation with a transmission distance on the order of the wavelength or less than wavelength to be realized. This can be further applied to design a few-layer metasurface or metamaterial optical devices, providing an alternative solution for all-optical light-field processing of both far-field and near-field optics.

For the experimental realization of the D²NN, an optical element that can simultaneously manipulate the phase and amplitude is required. A few-layer metasurface, which contains multiple functional layers, may be suitable to fabricate D²NN-based modulators. By designing the structural unit with two crystal-silicon nanoblocks, the metasurface can independently manipulate the phase and amplitude of light beams, which can be used as the neural layer of D²NNs [55]. However, the interlayer coupling in a few-layer metasurface may deteriorate the light-field-modulation performance by energy absorption and reflection in the dielectric surface. What is worse, the reflected beams between metasurfaces may interfere with each other, further imposing crosstalk on light beams. Therefore, few-layer metasurfaces may be suitable to construct a D²NN if the interlayer coupling effect can be suppressed, which needs further research.

V. CONCLUSION

In summary, we explore a D²NN-based all-optical signal-processing platform for VB manipulation, expanding the manipulation capability of light fields. By combining the light-field-manipulation capability of a multilayer diffraction structure and the memory, learning,

and information-processing ability of a deep neural network, D²NNs can establish an accurate mapping relationship between input and output beams, which significantly increases the accuracy of light-field modulation and the number of tolerable modes. By our training a five-layer D²NN with the ability to manipulate the spatial location and mode, VBs with $l \in [-8, +8]$ and Gaussian beams at different positions are mutually converted, and different OAM modes are exchanged, with the diffraction efficiency and purity reaching more than 96%. After being trained, D²NNs with the functions of hybrid-OAM-mode generation, detection, and switching are obtained, and three typical types of all-optical signal-processing communication (OAM-SK, OAM multiplexing and demultiplexing, and OAM-mode switching) are successfully achieved in simulation. It is anticipated that this D²NN method may open an alternative avenue for optical communication and interconnection due to its powerful light-field-manipulation capability.

ACKNOWLEDGMENTS

This work was funded by the National Natural Science Foundation of China (61805149, 61805087, 12047539); Guangdong Natural Science Foundation (2020A1515011392, 2019A1515111153, 2018A030313368, 2016A030310065); Program of Fundamental Research of Shenzhen Science and Technology Plan (JCYJ20200109144001800, JCYJ20180507182035270, GJHZ20180928160407303); Science and Technology Planning Project of Guangdong Province (2016B050501005); Science and Technology Project of Shenzhen (ZDSYS201707271014468); International Collaborative Laboratory of 2D Materials for Optoelectronics Science and Technology (2DMOST2018003); China Postdoctoral Science Foundation (2020M682867).

APPENDIX A: LIGHT-FIELD PROCESSING BY A D²NN

Conventional electronic neural networks are formed by interconnecting massive neurons and simulating the

synapse behaviors in human brains, and the information-processing speed is limited by electron flow. The optical D²NN takes the light fields as the information-processing object, and possesses the same learning and memory ability as electronic neural networks. The D²NN contains one input layer, multiple diffractive layers, and one output layer (see Fig. 1). Each point in the diffractive layers can be regarded as a neuron and fully connects with the next layer. According to Rayleigh-Sommerfeld diffraction theory, each neuron is regarded as the source of a secondary wave, following the optical modes [50]:

$$w_n^L(x, y, z) = \frac{z - z_n}{r_n^2} \left(\frac{1}{2\pi r_n} + \frac{1}{j\lambda} \right) \exp \left(\frac{j 2\pi r_n}{\lambda} \right), \quad (\text{A1})$$

where L represents the layers of the network, n represents the neuron located at (x_n, y_n, z_n) , $r_n = \sqrt{(x - x_n)^2 + (y - y_n)^2 + (z - z_n)^2}$, $j^2 = -1$, and λ is the working wavelength. The amplitude and phase of the secondary wave are determined by the input wave of neurons and the transmission coefficient $t_n^L(x_n, y_n, z_n)$. The output function of the n th neuron in the L th layer can be described as

$$n_n^L(x_n, y_n, z_n) = w_n^L(x_n, y_n, z_n) t_n^L(x_n, y_n, z_n) \times \sum_k n_k^{L-1}(x_n, y_n, z_n), \quad (\text{A2})$$

where the impact of the input wave on the n th neuron is described by $\sum_k n_k^{L-1}(x_n, y_n, z_n)$. Considering the optical characteristics, the light fields are manipulated by both the amplitude and phase, and Eq. (A2) can be simplified to

$$n_n^L(x_n, y_n, z_n) = w_n^L(x_n, y_n, z_n) |A| \exp[j \theta(x_n, y_n, z_n)], \quad (\text{A3})$$

where $|A|$ and $\theta(x_n, y_n, z_n)$ refer to the relative amplitude and additional phase delay of the secondary wave caused by the input wave and transmission coefficient. The secondary waves of neurons in the previous layer will interfere with each other and be diffracted and then propagate to the next layer until the output layer. D²NNs can be classified as phase-modulated, amplitude-modulated, and phase-modulated and amplitude-modulated types according to the transmission coefficient $t_n^L(x_n, y_n, z_n)$.

The theoretical derivation proves that the spiral phase structure is preserved when VBs propagate in free space [56], and the transmission results simulated by Fresnel scalar diffraction theory are consistent with the experimental results [19]. Therefore, Fresnel scalar diffraction theory is used in this work to construct the forward-propagation model of D²NNs to simulate the propagation between layers. The frequency description of incident beams at the

$(L-1)$ th layer can be expressed as

$$U_{z_{L-1}}^{L-1}(f_x, f_y) = \mathcal{F}(u_{z_{L-1}}^{L-1}(x_{L-1}, y_{L-1})), \quad (\text{A4})$$

where \mathcal{F} represents the fast Fourier transform, z_{L-1} is the observation plane on the propagation axis, and $u_{z_{L-1}}^{L-1}(x_{L-1}, y_{L-1})$ is the light field of the $(L-1)$ th layer in the spatial domain, and its expression in frequency is $U_{z_{L-1}}^{L-1}(f_x, f_y)$. Considering the transmission in the $(L-1)$ th layer, Eq. (A4) should be modified to

$$U_{z_{L-1}}^{L-1}(f_x, f_y) = \mathcal{F}(u_{z_{L-1}}^{L-1}(x_{L-1}, y_{L-1}) t_{z_{L-1}}^{L-1}(x_{L-1}, y_{L-1})). \quad (\text{A5})$$

According to Fresnel diffraction theory, the beam propagating to the L th layer can be described by multiplying the transform function $H(f_x, f_y)$ in the frequency domain, and the light field can be expressed by

$$u_{z_L}^L(x_L, y_L) = \mathcal{F}^{-1}(U_{z_{L-1}}^{L-1}(f_x, f_y) H(f_x, f_y)), \quad (\text{A6})$$

where $H(f_x, f_y) = \exp[jk(z_L - z_{L-1})] \exp[-j\pi\lambda(z_L - z_{L-1})(f_x^2 + f_y^2)]$, where $k = 2\pi/\lambda$ represents the wave number and $z_L - z_{L-1} = d$ is the distance between cascading diffractive layers, and \mathcal{F}^{-1} represents the reverse fast Fourier transform.

Here the size of the input plane, passive diffractive layers, and output plane are set as $30 \times 30 \text{ mm}^2$, with a resolution of 256×256 . The distance between each passive diffractive layer and the output layer is set as 30 mm. Each neuron of the layers fully connects with the next, and the neuron parameters in diffractive layers are computed by Google TensorFlow with a backward-propagation algorithm. The absolute-root-error function is selected to evaluate the difference between the output light fields predicted by scalar diffraction theory and the ideal output light fields of the D²NN, which can be expressed as

$$E_r = \sqrt{|Y_o - Y_i|}, \quad (\text{A7})$$

where Y_o and Y_i represent the actual and ideal output fields of the D²NN, respectively. The Adam gradient-descent algorithm is used to minimize the error function while the neurons are updated in diffractive layers.

APPENDIX B: CODING PRINCIPLE OF OAM-SK

In the modulation of OAM-shift keying, we select arbitrary four OAM modes with $l \in [-4, +4]$ to encode the pixel values, and an eight-bit binary number [see Fig. 20(a)] is used to represent the OAM modes to reduce coding complexity. There are a total of 70 (C_8^4) sets of hybrid VBs when four arbitrary bits from right to left are set as “1” and the rest are “0,” indicating that the D²NN is capable of 70-ary OAM-shift-keying modulation.

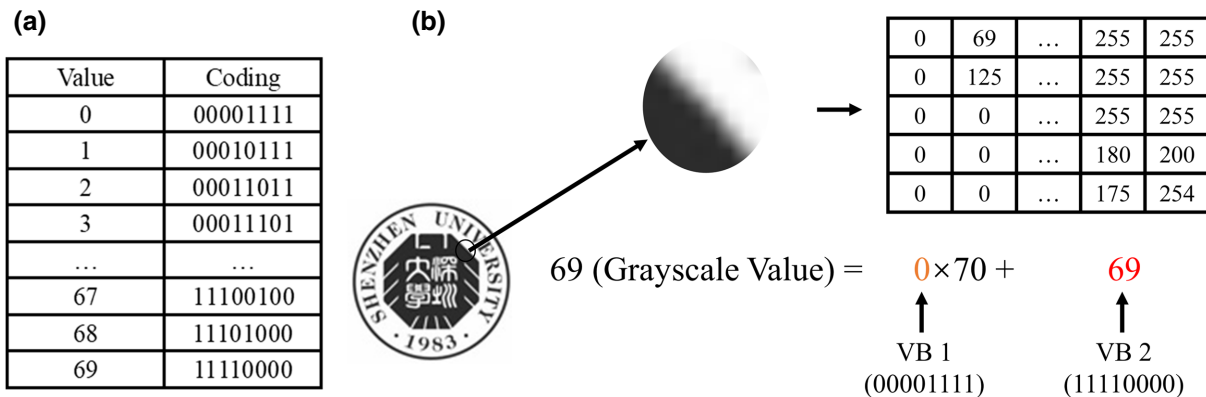


FIG. 20. Coding principle of OAM-shift keying. (a) The 70-ary mapping relationship between grayscale values and the hybrid VB. (b) Coding diagram of the grayscale image.

To represent all the pixel values, two sets of hybrid VBs are required for coding single grayscale values, and each grayscale value can be decomposed as

$$G = 70 \times m + n, \quad (\text{B1})$$

where G represents the grayscale value, m and n represent two coding bits. As shown in Fig. 20(b), the 100×100 Shenzhen University emblem can be regarded as a matrix with grayscale values, and it can be decomposed into a sequence composed of 20 000 hybrid VBs for transmission. For example, the grayscale value “69” is encoded into two hybrid VBs with $l = -1, +2, +3, +4$ ($m = 1$, 00010111) and $l = +1, +2, +3, +4$ ($n = 0$, 00001111).

- [1] L. Allen, M. W. Beijersbergen, R. J. C. Spreeuw, and J. P. Woerdman, Orbital angular momentum of light and the transformation of laguerre-Gaussian laser modes, *Phys. Rev. A* **45**, 8185 (1992).
- [2] M. Woerdemann, C. Alpmann, and C. Denz, Optical assembly of microparticles into highly ordered structures using ince-Gaussian beams, *Appl. Phys. Lett.* **98**, 111101 (2011).
- [3] M. Padgett and R. Bowman, Tweezers with a twist, *Nat. Photonics* **5**, 343 (2011).
- [4] R. Fickler, R. Lapkiewicz, W. N. Plick, M. Krenn, C. Schaeff, S. Ramelow, and A. Zeilinger, Quantum entanglement of high angular momenta, *Science (80-.)* **338**, 640 (2012).
- [5] R. Fickler, R. Lapkiewicz, M. Huber, M. P. J. Lavery, M. J. Padgett, and A. Zeilinger, Interface between path and orbital angular momentum entanglement for high-dimensional photonic quantum information, *Nat. Commun.* **5**, 4502 (2014).
- [6] M. Woerdemann, C. Alpmann, M. Esseling, and C. Denz, Advanced optical trapping by complex beam shaping, *Laser Photon. Rev.* **7**, 839 (2013).
- [7] X. Zhou Cui, X. Li Yin, H. Chang, Y. Lin Guo, Z. Jian Zheng, Z. Wen Sun, G. Yao Liu, and Y. Jun Wang, Analysis of an adaptive orbital angular momentum shift keying decoder

based on machine learning under oceanic turbulence channels, *Opt. Commun.* **429**, 138 (2018).

- [8] S. Lohani and R. T. Glasser, Turbulence correction with artificial neural networks, *Opt. Lett.* **43**, 2611 (2018).
- [9] J. Liu, P. Wang, X. Zhang, Y. He, X. Zhou, H. Ye, Y. Li, S. Xu, S. Chen, and D. Fan, Deep learning based atmospheric turbulence compensation for orbital angular momentum beam distortion and communication, *Opt. Express* **27**, 16671 (2019).
- [10] P. Wang, J. Liu, L. Sheng, Y. He, Z. Huang, X. Zhou, Y. Li, S. Chen, X. Zhang, and D. Fan, Convolutional neural network-assisted optical orbital angular momentum recognition and communication, *IEEE Access* **7**, 162025 (2019).
- [11] T. Doster and A. T. Watnik, Machine learning approach to OAM beam demultiplexing via convolutional neural networks, *Appl. Opt.* **56**, 3386 (2017).
- [12] Z. Huang, P. Wang, J. Liu, W. Xiong, Y. He, X. Zhou, J. Xiao, Y. Li, S. Chen, and D. Fan, Identification of hybrid orbital angular momentum modes with deep feedforward neural network, *Results Phys.* **15**, 102790 (2019).
- [13] Y. He, J. Liu, P. Wang, W. Xiong, Y. Wu, X. Zhou, Y. Cheng, Y. Gao, Y. Li, S. Chen, and D. Fan, Detecting orbital angular momentum modes of vortex beams using feed-forward neural network, *J. Light. Technol.* **37**, 5848 (2019).
- [14] S. Lohani, E. M. Knutson, M. O'Donnell, S. D. Huver, and R. T. Glasser, On the Use of deep neural networks in optical communications, *Appl. Opt.* **57**, 4180 (2018).
- [15] Q. Tian, Z. Li, K. Hu, L. Zhu, X. Pan, Q. Zhang, Y. Wang, F. Tian, X. Yin, and X. Xin, Turbo-Coded 16-Ary OAM shift keying FSO communication system combining the CNN-based adaptive demodulator, *Opt. Express* **26**, 27849 (2018).
- [16] N. Bozinovic, Y. Yue, Y. Ren, M. Tur, P. Kristensen, H. Huang, A. E. Willner, and S. Ramachandran, Terabit-Scale orbital angular momentum mode division multiplexing in fibers, *Science (80-.)* **340**, 1545 (2013).
- [17] H. Huang, G. Xie, Y. Yan, N. Ahmed, Y. Ren, Y. Yue, D. Rogawski, M. J. Willner, B. I. Erkmen, K. M. Birnbaum,

- S. J. Dolinar, M. P. J. Lavery, M. J. Padgett, M. Tur, and A. E. Willner, 100 tbit/s free-space data link enabled by three-dimensional multiplexing of orbital angular momentum, polarization, and wavelength, *Opt. Lett.* **39**, 197 (2014).
- [18] L. Li, G. Xie, Y. Ren, N. Ahmed, H. Huang, Z. Zhao, P. Liao, M. P. J. Lavery, Y. Yan, C. Bao, Z. Wang, A. J. Willner, N. Ashrafi, S. Ashrafi, M. Tur, and A. E. Willner, Orbital-Angular-Momentum-Multiplexed free-space optical communication link using transmitter lenses, *Appl. Opt.* **55**, 2098 (2016).
- [19] J. Wang, J. Y. Yang, I. M. Fazal, N. Ahmed, Y. Yan, H. Huang, Y. Ren, Y. Yue, S. Dolinar, M. Tur, and A. E. Willner, Terabit free-space data transmission employing orbital angular momentum multiplexing, *Nat. Photonics* **6**, 488 (2012).
- [20] A. Longman and R. Fedosejevs, Mode conversion efficiency to laguerre-Gaussian OAM modes using spiral phase optics, *Opt. Express* **25**, 17382 (2017).
- [21] H. Cai, S. Chen, C. Zou, Q. Huang, Y. Liu, X. Hu, Z. Fu, Y. Zhao, H. He, and Y. Lu, Multifunctional hybrid metasurfaces for dynamic tuning of terahertz waves, *Adv. Opt. Mater.* **6**, 1 (2018).
- [22] P. Huo, C. Zhang, W. Zhu, M. Liu, S. Zhang, S. Zhang, L. Chen, H. J. Lezec, A. Agrawal, Y. Lu, and T. Xu, Photonic spin-multiplexing metasurface for switchable spiral phase contrast imaging, *Nano Lett.* **20**, 2791 (2020).
- [23] P. Huo, Y. Liang, S. Zhang, Y. Lu, and T. Xu, Angular optical transparency induced by photonic topological transitions in metamaterials, *Laser Photonics Rev.* **12**, 1 (2018).
- [24] Z. Jin, S. Mei, S. Chen, Y. Li, C. Zhang, Y. He, X. Yu, C. Yu, J. K. W. Yang, B. Luk'Yanchuk, S. Xiao, and C. W. Qiu, Complex inverse design of meta-optics by segmented hierarchical evolutionary algorithm, *ACS Nano* **13**, 821 (2019).
- [25] J. Li, S. Kamin, G. Zheng, F. Neubrech, S. Zhang, and N. Liu, Addressable metasurfaces for dynamic holography and optical information encryption, *Sci. Adv.* **4**, 1 (2018).
- [26] X. Luo, Subwavelength optical engineering with metasurface waves, *Adv. Opt. Mater.* **6**, 1 (2018).
- [27] Y. Chen, K. Y. Xia, W. G. Shen, J. Gao, Z. Q. Yan, Z. Q. Jiao, J. P. Dou, H. Tang, Y. Q. Lu, and X. M. Jin, Vector Vortex Beam Emitter Embedded in a Photonic Chip, *Phys. Rev. Lett.* **124**, 153601 (2020).
- [28] F. Zhang, M. Pu, X. Li, P. Gao, X. Ma, J. Luo, H. Yu, and X. Luo, All-Dielectric metasurfaces for simultaneous giant circular asymmetric transmission and wavefront shaping based on asymmetric photonic spin-orbit interactions, *Adv. Funct. Mater.* **27**, 1 (2017).
- [29] Q. Feng, M. Pu, C. Hu, and X. Luo, Engineering the dispersion of metamaterial surface for broadband infrared absorption, *Opt. Lett.* **37**, 2133 (2012).
- [30] P. Huo, S. Zhang, Y. Liang, Y. Lu, and T. Xu, Hyperbolic metamaterials and metasurfaces: Fundamentals and applications, *Adv. Opt. Mater.* **7**, 1 (2019).
- [31] H. Cai, Q. Huang, X. Hu, Y. Liu, Z. Fu, Y. Zhao, H. He, and Y. Lu, All-Optical and ultrafast tuning of terahertz plasmonic metasurfaces, *Adv. Opt. Mater.* **6**, 1 (2018).
- [32] S. Jiang, C. Chen, H. Zhang, and W. Chen, Achromatic electromagnetic metasurface for generating a vortex wave with orbital angular momentum (OAM), *Opt. Express* **26**, 6466 (2018).
- [33] X. Ma, M. Pu, X. Li, C. Huang, Y. Wang, W. Pan, B. Zhao, J. Cui, C. Wang, Z. Zhao, and X. Luo, A planar chiral meta-surface for optical vortex generation and focusing, *Sci. Rep.* **5**, 1 (2015).
- [34] Y. Liu, X. Ling, X. Yi, X. Zhou, H. Luo, and S. Wen, Realization of polarization evolution on higher-order poincaré sphere with metasurface, *Appl. Phys. Lett.* **104**, 191110 (2014).
- [35] Y. He, P. Wang, C. Wang, J. Liu, H. Ye, X. Zhou, Y. Li, S. Chen, X. Zhang, and D. Fan, All-Optical signal processing in structured light multiplexing with dielectric meta-optics, *ACS Photonics* **7**, 135 (2019).
- [36] F. Bi, Z. Ba, and X. Wang, Metasurface-Based broadband orbital angular momentum generator in millimeter wave region, *Opt. Express* **26**, 25693 (2018).
- [37] J. Zhou, H. Qian, C. Chen, J. Zhao, G. Li, Q. Wu, H. Luo, S. Wen, and Z. Liu, Optical edge detection based on high-efficiency dielectric metasurface, *Proc. Natl. Acad. Sci. U. S. A.* **116**, 11137 (2019).
- [38] F. Qin, L. Wan, L. Li, H. Zhang, G. Wei, and S. Gao, A transmission metasurface for generating OAM beams, *IEEE Antennas Wirel. Propag. Lett.* **17**, 1793 (2018).
- [39] S. Yu, L. Li, G. Shi, C. Zhu, X. Zhou, and Y. Shi, Design, fabrication, and measurement of reflective metasurface for orbital angular momentum vortex wave in radio frequency domain, *Appl. Phys. Lett.* **108**, 1 (2016).
- [40] M. L. N. Chen, L. J. Jiang, and W. E. I. Sha, Ultrathin complementary metasurface for orbital angular momentum generation at microwave frequencies, *IEEE Trans. Antennas Propag.* **65**, 396 (2017).
- [41] F. Brandt, M. Hiekkämäki, F. Bouchard, M. Huber, and R. Fickler, High-Dimensional quantum gates using full-field spatial modes of photons, *Optica* **7**, 98 (2020).
- [42] N. K. Fontaine, R. Ryf, H. Chen, D. T. Neilson, K. Kim, and J. Carpenter, Laguerre-Gaussian mode sorter, *Nat. Commun.* **10**, 1 (2019).
- [43] J. F. Morizur, P. Jian, B. Denolle, O. Pinel, N. Barré, and G. Labroille, Efficient and mode-selective spatial multiplexer based on multi-plane light conversion, *Opt. Fiber Commun. Conf. OFC* **22**, 488 (2015).
- [44] Y. Sakamaki, T. Saida, T. Hashimoto, and H. Takahashi, New optical waveguide design based on wavefront matching method, *J. Light. Technol.* **25**, 3511 (2007).
- [45] D. Liao, K. F. Chan, C. H. Chan, Q. Zhang, and H. Wang, All-Optical diffractive neural networked terahertz hologram, *Opt. Lett.* **45**, 2906 (2020).
- [46] T. Zhou, L. Fang, T. Yan, J. Wu, Y. Li, J. Fan, H. Wu, X. Lin, and Q. Dai, In situ optical backpropagation training of diffractive optical neural networks, *Photonics Res.* **8**, 940 (2020).
- [47] Y. Zuo, B. Li, Y. Zhao, Y. Jiang, Y.-C. Chen, P. Chen, G.-B. Jo, J. Liu, and S. Du, All-Optical neural network with nonlinear activation functions, *Optica* **6**, 1132 (2019).
- [48] J. Feldmann, N. Youngblood, C. D. Wright, H. Bhaskaran, and W. H. P. Pernice, All-Optical spiking neurosynaptic networks with self-learning capabilities, *Nature* **569**, 208 (2019).

- [49] S. Jiao, J. Feng, Y. Gao, T. Lei, Z. Xie, and X. Yuan, Optical machine learning with incoherent light and a single-pixel detector, *Opt. Lett.* **44**, 5186 (2019).
- [50] C. Qian, X. Lin, X. Lin, J. Xu, Y. Sun, E. Li, B. Zhang, and H. Chen, Performing optical logic operations by a diffractive neural network, *Light Sci. Appl.* **9**, 1 (2020).
- [51] T. Yan, J. Wu, T. Zhou, H. Xie, F. Xu, J. Fan, L. Fang, X. Lin, and Q. Dai, Fourier-space Diffractive Deep Neural Network, *Phys. Rev. Lett.* **123**, 23901 (2019).
- [52] X. Lin, Y. Rivenson, N. T. Yardimci, M. Veli, Y. Luo, M. Jarrahi, and A. Ozcan, All-optical machine learning using diffractive deep neural networks, *Science (80-.)* **361**, 1004 (2018).
- [53] J. Vickers, M. Burch, R. Vyas, and S. Singh, Phase and interference properties of optical vortex beams, *J. Opt. Soc. Am. A Opt. Image Ence Vis.* **25**, 823 (2008).
- [54] L. C. Andrews and R. L. Phillips, *Laser Beam Propagation Through Random Media* (SPIE, Bellingham, Washington, 2005).
- [55] Y. Bao, J. Ni, and C.-W. Qiu, A minimalist single-layer metasurface for arbitrary and full control of vector vortex beams, *Adv. Mater.* **32**, 1905659 (2020).
- [56] G. Indebetouw, Optical vortices and their propagation, *J. Mod. Opt.* **40**, 73 (1993).